# Interplay of charge and spin fluctuations of strongly interacting electrons on the kagome lattice

Frank Pollmann,[1,*] Krishanu Roychowdhury,[1] Chisa Hotta,[2,3] and Karlo Penc[4]
[1]*Max-Planck-Institut für Physik komplexer Systeme, 01187 Dresden, Germany*
[2]*Department of Physics, Faculty of Science, Kyoto Sangyo University, Kyoto 603-8555, Japan*
[3]*Department of Basic Science, University of Tokyo, 3-8-1 Komaba, Meguro, Tokyo 153-8902, Japan*
[4]*Institute for Solid State Physics and Optics, Wigner Research Centre for Physics, Hungarian Academy of Sciences, P.O. Box 49, H-1525 Budapest, Hungary*
(Received 12 March 2014; published 14 July 2014)

We study electrons hopping on a kagome lattice at third filling described by an extended Hubbard Hamiltonian with on-site and nearest-neighbor repulsions in the strongly correlated limit. As a consequence of the commensurate filling and the large interactions, each triangle has precisely two electrons in the effective low-energy description, and these electrons form chains of different lengths. The effective Hamiltonian includes the ring exchange around the hexagons as well as the nearest-neighbor Heisenberg interaction. Using large-scale exact diagonalization, we find that the effective model exhibits two phases: If the charge fluctuations are small, the magnetic fluctuations confine the charges to short loops around hexagons, yielding a gapped charge-ordered phase. When the charge fluctuations dominate, the system undergoes a quantum phase transition to a resonating plaquette phase with ordered spins and gapless spin excitations. We find that a peculiar conservation law is fulfilled: the electron in the chains can be divided into two sublattices, and this division is conserved by the ring exchange term.

DOI: 10.1103/PhysRevB.90.035118 PACS number(s): 71.10.Fd, 75.10.Jm, 71.10.Hf

## I. INTRODUCTION

Strongly correlated systems on frustrated lattices can exhibit very interesting physics. The competition between different interactions often results in multiple low-energy states which are degenerate or nearly degenerate with each other. Consequently, quantum fluctuations become very important at low temperatures and can lead to emergent phases of matter with exotic properties.

One such example is spin ice on the pyrochlore lattice, which hosts collective excitations that form magnetic monopoles [1]. At very low temperatures, where quantum fluctuations become important, these models have been shown to stabilize an artificial quantum electrodynamics, supporting magnetic and electric charges as well as linearly dispersing, gapless excitations (photons) [2–5]. Another exciting example is the quantum Heisenberg model on the kagome lattice [6], which is believed to exhibit a $\mathbb{Z}_2$ topological liquid ground state, carrying anyonic excitations [7–9]. Recently, indications for the existence of a $\mathbb{Z}_3$ spin liquid have been observed when a finite magnetic field is applied [10]. Both examples are systems involving localized spins. The effect of frustration on charge degrees of freedom has received less attention so far. Still, in a number of recent works, it has been shown that models at partial filling (i.e., itinerant systems) on frustrated lattices support fractional charges in two and three dimensions [11–14]. This fact is quite interesting, as there exist only a few examples of models that support fractional charges in higher dimensions. One very interesting and important question is about the interplay of spin and charge degrees of freedom. For a checkerboard lattice model at quarter-filling, the interplay between charge and spin degrees of freedom can stabilize a robust insulating resonating singlet-pair crystal phase [15,16]. Previous studies on the kagome lattice at different filling factors have revealed rich phase diagrams including various symmetry-broken as well as topological phases [17,18]. At filling factor $1/6$, a new mechanism for ferromagnetism on the kagome lattice was found [19].

In this paper, we study the interplay between spin and charge degrees of freedom on the kagome lattice at a filling factor of $n = 2/3$. Most interestingly, we find that the spin fluctuation in the model can drive the systems through a phase transition into a charge-ordered phase. We start from an extended Hubbard model on the kagome lattice for which we derive a low-energy Hamiltonian using degenerate perturbation theory. By considering different limiting cases, we obtain some insight into the different phases of the model. In the limit where antiferromagnetic spin fluctuations dominate, a "short-loop" phase is formed in which the charges align around hexagons. On the other hand, if the charge fluctuations dominate, we find a "plaquette-ordered" ground state. For the latter limit (no spin fluctuations), we find a very peculiar conservation law, namely, the Hamiltonian conserves the magnetization on dynamic sublattices. To get a picture of the whole phase diagram, we perform a large-scale exact diagonalization study of clusters up to $N = 36$ sites in which we calculate the energy spectrum and different correlation functions from which we conclude the phase diagram.

This paper is organized as follows: In Sec. II, we introduce the model Hamiltonian and derive the low-energy effective Hamiltonian. We then consider the limiting cases in Sec. III, allowing us to make some statements about some corners of the phase diagram. The full phase diagram is then evaluated using exact diagonalization in Sec. IV. We conclude by giving a short summary and outlook in Sec. V.

*frankp@pks.mpg.de

 

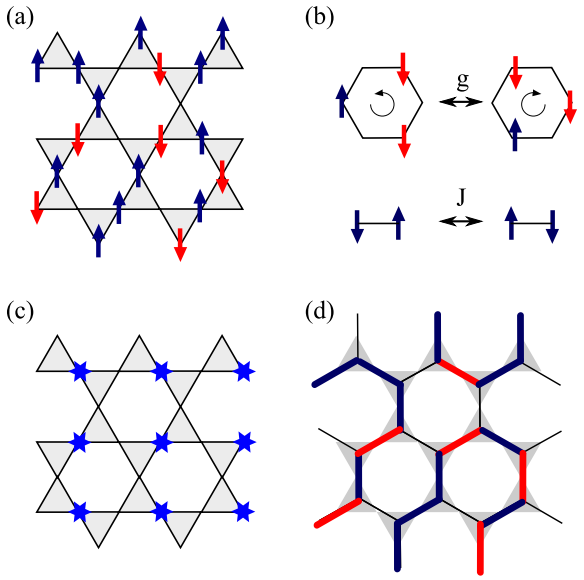


FIG. 1. (Color online) (a) A configuration satisfying the constraint of zero or one electron per site and two electrons of arbitrary spin per triangle. (b) Quantum fluctuations allow tunneling between different degenerate configurations of spins and charge: ring exchange with amplitude $g$ and spin-exchange with an amplitude of $J$. The ring exchange processes change the number of electrons on the starred (blue) sublattice shown in (c), always by two. This is crucial for gauging away the sign of $g$ explained in the text. (d) All allowed configurations can be expressed in terms of a two-colored fully packed loop model on the honeycomb lattice; as an example, we show a representation of the configuration presented in (a).

## II. MODEL HAMILTONIAN

Here we consider the extended Hubbard model on a kagome lattice with on-site and nearest-neighbor repulsive interactions $U$ and $V$, respectively, with the Hamiltonian

$$\mathcal{H} = -t \sum_{\langle i,j\rangle,\sigma} (c^\dagger_{i\sigma} c_{j\sigma} + \text{H.c.}) + V \sum_{\langle i,j\rangle} n_i n_j + U \sum_i n_{i\uparrow} n_{i\downarrow}. \quad (1)$$

The operators $c_{i\sigma}$ ($c^\dagger_{i\sigma}$) annihilate (create) an electron with spin $\sigma$ at site $i$, $n_i = n_{i\uparrow} + n_{i\downarrow}$ is the electron number operator with $n_{i\sigma} = c^\dagger_{i\sigma} c_{i\sigma}$, and the notation $\langle i,j\rangle$ refers to pairs of nearest neighbors. Throughout this paper, we focus on the case of one-third filling, in the strongly correlated regime, where $|t| \ll V < U$. For this filling there are two electrons on each triangle on average (i.e., the total number of electrons is $N_e = 2N/3$, where $N$ is the number of lattice sites, providing a filing factor $n = N_e/N = 2/3$).

In the strong-coupling limit, when $t = 0$ and $U > V > 0$, the energy is minimized if there are *exactly* two electrons per each triangle of the kagome lattice with no double-occupancy: this is analogous to the case of magnetite as discussed in Ref. [20]. An example configuration fulfilling these constraints is shown in Fig. 1(a). The number of such configurations is macroscopically degenerate: in addition to the trivial $2^{2N/3}$ spin degeneracy, the number of charge configurations also grows exponentially with the system size. The ground-state configurations on the kagome lattice can be mapped to two-colored fully packed loop configurations on the honeycomb lattice [particles are sitting here on links of the honeycomb lattice, and the two different colors encode the spin orientation; see Fig. 1(d)]. The charge degrees of freedom (i.e., neglecting the color) can be equivalently described by a dimer model by exchanging the role of occupied and empty bonds. Using this mapping, the degeneracy of different charge configurations can be calculated exactly using Pfaffians [21] and is given as $\sim 1.1137^N$ for a honeycomb lattice with $N$ bonds (corresponding to $N$ kagome sites). The total degeneracy is then the product of the spin degeneracy and the charge degeneracy; i.e., $\sim 2^{2N/3} \times 1.1137^N$.

The macroscopic ground-state degeneracy is lifted when quantum fluctuations are taken into account. The effective Hamiltonian that connects a manifold of degenerate states can be obtained from a perturbative expansion of the Hamiltonian, Eq. (1), in $t/V$ and $t/(U-V)$. By keeping only the lowest order of nonvanishing terms, one obtains the effective Hamiltonian as the sum of two parts:

$$\mathcal{H}_{\text{eff}} = \mathcal{H}_{\text{ring}} + \mathcal{H}_{\text{spin}}. \quad (2)$$

The first term describes a ring exchange of three electrons occupying every other site on a hexagon of the kagome lattice and is given as

$$\mathcal{H}_{\text{ring}} = -g \sum_{\{\hexagon\}} h_{\hexagon}, \quad (3)$$

with an effective ring-exchange amplitude $g = 6t^3/V^2$ and

$$h_{\hexagon} = \sum_{\{\sigma,\sigma',\sigma''\}} (c^\dagger_{n\sigma''} c_{m\sigma''} c^\dagger_{l\sigma'} c_{k\sigma'} c^\dagger_{j\sigma} c_{i\sigma} + \text{H.c.}). \quad (4)$$

The sum is performed over sites of the hexagon and all spin orientations. The indices $i$, $j$, $k$, $l$, $m$, and $n$ are sites oriented clockwise on a hexagon yielding the dynamics sketched in Fig. 1(b); i.e., three electrons hop collectively either clockwise or counterclockwise around the hexagons. Clearly, this ring exchange process preserves the number of electrons on each triangle, and if applied to a state that belongs to the ground-state manifold, the resulting state will also belong to the same manifold. Note that the fermionic sign in expression for $\mathcal{H}_{\text{ring}}$ can be gauged away, yielding a bosonic model [14]. Furthermore, the overall sign of $g$ can be transformed by a simple gauge transformation which multiplies all configurations by the factor $i^{N_{\text{star}}}$, where $N_{\text{star}}$ is the number of electrons on the sublattice shown in Fig. 1(c).

The second term in the effective Hamiltonian, (2), is the nearest-neighbor Heisenberg exchange

$$\mathcal{H}_{\text{spin}} = J \sum_{\langle i,j\rangle} \left(2 S_i S_j - \frac{1}{2} n_i n_j\right), \quad (5)$$

where

$$J = \frac{2t^2}{U-V} + \frac{2t^3}{V^2}. \quad (6)$$

In the ground-state manifold, each electron has two occupied neighboring sites (one on each of the two corner-sharing triangles), so that closed loops are formed in a system with

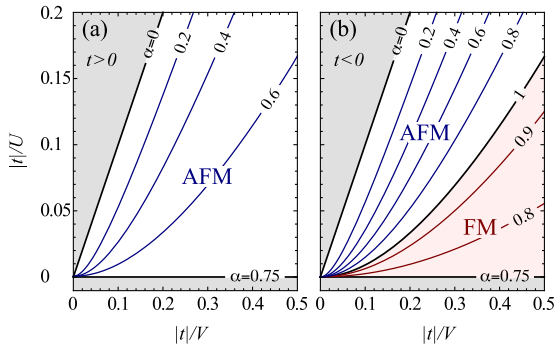


FIG. 2. (Color online) Values of the parameter $\alpha$ defined in Eq. (7) as contour plots on the plane of $|t|/U$ and $|t|/V$. (a) For $t > 0$ the exchange is always antiferromagnetic, while (b) for $t < 0$ the exchange becomes ferromagnetic [shaded (pink) region] for large on-site repulsion $U$, as it follows from the perturbative expansion up to third order in the hopping, Eq. (6). The effective Hamiltonian describes the region close to the origin in the unshaded (white) region $U > V$ and $U > 0$.

periodic boundary conditions. These loops are like spin chains and the exchange Hamiltonian $\mathcal{H}_{\text{spin}}$ acts on the spins of the electrons in these closed loops without modifying the charge configuration. The length of the loops is always even, and the shortest loop length is 6. For $U \gg V$ the first term in Eq. (6), proportional to $t^2$, becomes small compared to the term that is $\propto t^3$, so that the sign of the exchange depends on the sign of the hopping amplitude $t$, allowing antiferromagnetic as well as ferromagnetic exchanges (analogously to the one-dimensional case considered in Ref. [22]). One important aspect of the effective model, Eq. (2), is that $g$ and $J$ can be regarded as nearly independent variables: One can tune the value of $J$ by changing $U$, without affecting $g$. We can reparametrize them by a single variable,

$$\alpha = \frac{|g|}{|g| + |J|}, \tag{7}$$

which falls within $0 \leqslant \alpha \leqslant 1$. In the limiting case $\alpha \to 0$ we can neglect the effect of the ring exchange term. This happens when $V \to U$ (but still $V > U$), as due to the divergence in Eq. (6), the effective exchange becomes much larger than $g$. In the limit of $V \ll U$, $\alpha$ approaches $\alpha \to 3/4$ as

$$\alpha = \frac{3}{4} - \frac{3V^2}{16tU} + O(1/U^2). \tag{8}$$

However, the overall behavior is not as simple and in the following we consider the different signs of the hopping $t$ separately: Figures 2(a) and 2(b) show contour plots of $\alpha$ on the plane $U$ and $V$ (more precisely, $t/U$ and $t/V$) for $t > 0$ and $t < 0$, respectively.

For $t > 0$, the exchange is always antiferromagnetic and $0 < \alpha \leqslant 3/4$. To increase $\alpha$ from the $\alpha = 0$ limit at $U = V$, we need to increase $U$ compared to $V$, and from Eq. (8) we find the upper bound as $3/4$.

The situation is more involved when $t < 0$: we encounter both ferromagnetic and antiferromagnetic $J$, and $\alpha$ can take values $0 < \alpha \leqslant 1$. The line $\alpha = 1$ in Fig. 2(b) is determined by the antiferromagnetic $\propto t^2$ term, canceling the ferromagnetic $\propto t^3$ term in $J$ [see Eq. (6)]. When the effective exchange is ferromagnetic, the values of $\alpha$ are limited to $3/4 \leqslant \alpha < 1$: as $U$ increases from the $\alpha = 1$ line, $\alpha$ decreases down to $3/4$ for $U \gg V$ [Eq. (8)]. The antiferromagnetic exchange is realized by decreasing $U$ from the $\alpha = 1$ line toward $U = V$, which decreases $\alpha$ down to 0. These factors indicate that, with a suitable choice of the values of interactions and hoppings, we can select antiferromagnetic exchange with arbitrary value of $0 < \alpha < 1$.

Here, let us mention that we can link our model to the "flat-band" ferromagnetism: the Hubbard model with $t > 0$ and $n \leqslant 1/3$ has been proven to be ferromagnetic for any $U > 0$ and $V = 0$ [23,24]. Furthermore, the $n = 1/3$ case with $|t| \ll V \ll U$ is also proven to exhibit a ferromagnetic ground state [19]; thus here we extend the possibility of a ferromagnetic ground state also to filling factor $n = 2/3$.

In the remainder of the paper, we consider how the effective Hamiltonian lifts the degeneracy of the ground-state manifold in the strong-coupling limit.

## III. LIMITING CASES

It is instructive to first consider the two terms in the effective Hamiltonian, Eq. (2) separately. This corresponds to the setting $\alpha = 1$ and $\alpha = 0$. Understanding these two limits will help us get a picture of the full phase diagram.

### A. Plaquette phase of the ring exchange Hamiltonian ($\alpha = 1$)

At $\alpha = 1$, the effective Hamiltonian reduces to $\mathcal{H}_{\text{ring}}$ given by Eq. (3). First, we use the mapping to the two-color fully packed loop model [see Fig. 1(d)] to understand the charge dynamics. Second, we discuss a hidden symmetry of this model that yields large degeneracies.

#### *1. Resonating plaquettes and winding numbers*

When the spins of the electrons are all pointing in the same direction (e.g., up; $S = S^z = S_{\text{tot}}^{\text{max}}$), the spins can be omitted and the relevant degrees of freedom are the positions of the charges. As described in Sec. II, the charge problem can be mapped to a dimer model on the honeycomb lattice. The quantum-dimer model on the honeycomb lattice with resonances on the neighboring disjunct hexagons has been shown to have a gapped, plaquette-ordered ground state with an off–diagonal order parameter [25]: the so-called "plaquette phase." The ground state is threefold degenerate in the thermodynamic limit, breaking the translational symmetry of the lattice. The plaquette phase, when mapped back to the kagome lattice model, hosts electrons resonating around the hexagons (see Fig. 8, right). Then, one can define conserved quantities (winding numbers) that can be used to classify the states in the Hilbert space, similar to the quantum-dimer model on a square lattice [26]. In our case, $\mathcal{H}_{\text{ring}}$ conserves the number of electrons along the straight lines parallel to the edges of the hexagons in the kagome lattice. Actually, the number of linearly independent winding numbers is only two when the system is put onto a torus (i.e., when considering standard periodic boundary conditions). The Hilbert space is divided into subspaces (sectors), as only states having the same winding numbers are connected by $\mathcal{H}_{\text{ring}}$.

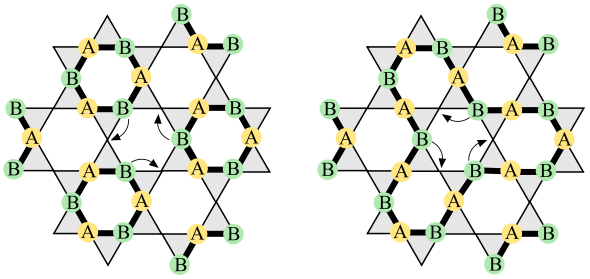


FIG. 3. (Color online) Dynamic sublattice structure defined on a loop of charges, consisting of an even number of sites. The effective ring exchange denoted by arrows preserves the magnetization on each of the dynamic sublattices $A$ and $B$ (see Appendix A for details).

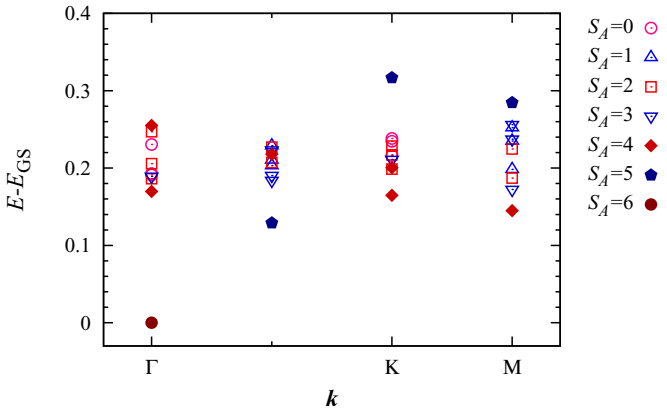


FIG. 4. (Color online) Energy spectrum of the $N = 36$ cluster at $\alpha = 1$. We set one of the two dynamic sublattices to be fully polarized as $S_B = 6$ while varying the spin $S_A$ of the other sublattice. The ground state is realized at the $\Gamma$ point for $S_A = 6$, indicating that both dynamic sublattices hold maximal spins.

### 2. *Hidden conservation law*

In what follows, we investigate the effect of the ring exchange on the spins of electrons in the loops. We show that, in addition to the trivial conservation of the total $z$ component $S^z_{\rm tot}$ and the total spin $S_{\rm tot}$, a *hidden conservation law* emerges, which we describe below.

Let us introduce the *dynamic two-sublattices* which are defined on top of the electron loops (Fig. 3): starting from an arbitrary choice of the loop configuration of electrons, we assign the bipartite labels, $A$ and $B$, to each electron in the loop; this is possible because loops consist of even-number sites. To be more precise, the rules to construct the dynamic sublattice are simple: (i) neighboring electrons have different sublattice labels, and (ii) next-nearest-neighbor electrons have the same sublattice label on each hexagon of the kagome lattice. For example, we find hexagon configurations which are completely filled (*ABABAB* as we go around the hexagon) or depleted hexagons such as *AOAOAO*, *ABAOAO*, and *ABABAO* (here the $O$ denotes empty sites). Once we have the configuration which fulfills (i) and (ii), the effective Hamiltonian $\mathcal{H}_{\rm ring}$ conserves this rule: After operating $\mathcal{H}_{\rm ring}$ arbitrary times, one finds that the bipartite configuration is perfectly retained: each electron can be assigned not only the spin, but also the label denoting the dynamic sublattice. The proof of this conjecture is given in Appendix A. Here, note that even if we return to the same charge configuration at some point, the sites that were occupied by $A$ electrons could all be replaced with $B$ electrons, and vice versa. In fact, even though the bipartite sublattice rule is maintained in the loops, the absolute locations of $A$ and $B$ are not fixed, which is the reason we call them "dynamic."

Next, we assign the spins to the electrons in the loops. Since the electrons in the $A$ and $B$ sublattices never exchange with each other, the total $S^z_A$ and $S^z_B$ on each of the dynamic sublattices is a conserved quantity, so it is a good quantum number. This is true not only for the $z$ component, but also for $\mathbf{S}_A$ and $\mathbf{S}_B$. As a consequence, the Hilbert subspaces of a fixed winding number are further divided into sectors that do not mix the spin $S^z$ on the two sublattices. For a system with the magnetization $S_{\rm max} - n$ we find $\lfloor n/2 + 1 \rfloor$ disconnected sectors; e.g., if we take $S_{\rm max} - 2$, namely, flipping two spins from a fully spin polarized configuration, we can either flip both spins on one of the dynamic sublattices or one spin on each of the sublattices, yielding two disjoint sectors. In fact, by keeping $S^z_{\rm tot} = S^z_A + S^z_B$, the number $\lfloor n/2 + 1 \rfloor$ is equal to the number of ways in which one can add two integers.

The hidden conservation law yields a spin degeneracy. To show this, we introduce the $P_{AB}$ operator that exchanges the $A$ and $B$ sublattice labels of the electron operators (note that this operator does not change the charge configuration). Since $P^2_{AB} = 1$, the wave functions are either even or odd with respect to $P_{AB}$, with eigenvalues $\pm 1$. The ring exchange Hamiltonian and the $\mathbf{S}_A + \mathbf{S}_B$ commute with the $P_{AB}$, while the $\mathbf{S}_A - \mathbf{S}_B$ does not. However, we can define the operator,

$$Q^{\mu\nu} = \left(S^\mu_A - S^\mu_B\right)\left(S^\nu_A - S^\nu_B\right), \tag{9}$$

which commutes with both the $P_{AB}$ and the $\mathcal{H}_{\rm ring}$ (where $\mu, \nu = x, y, z$). The $Q^{\mu\nu}$ has nonvanishing matrix elements between total spin states that differ by 2, so these states are also degenerate in energy [more precisely, the $Q^{\mu\nu} + Q^{\nu\mu} - (2/3)\delta_{\mu\nu} Q^{\eta\eta}$ is a rank 2 tensor operator]. For example, applying the $Q^{--}$ to the highest weight state of the maximal spin we create a state that is a linear superposition of $S^{\rm max}_{\rm tot}$ and $S^{\rm max}_{\rm tot} - 2$ and is degenerate with the $S^{\rm max}$. Regarding the ground state, we find that the total spin on $A$ and $B$ dynamic sublattices is maximal, $S_A = S_B = N/6$. This could be observed explicitly for the cluster with $N = 36$ sites shown in Fig. 4: There, we keep one of the two sublattices polarized as $S_B = 6$ and vary the total spin of the other sublattice ($S_A$). We find that the ground state does in fact have a maximal $S_A$. The two "giant" spins can be combined to make $S^{\rm max}_{\rm tot} - 2m$ spin states that are even with respect to $P_{AB}$, all having the same minimal energy (here $m$ is an integer). Similarly, the $S^{\rm max}_{\rm tot} - 2m - 1$ are also degenerate and are odd eigenstates of $P_{AB}$. In other words, in the ground state the two giant spins on the two dynamic sublattices behave as noninteracting spins (except for the parity effect with respect to $P_{AB}$, which disappears in the thermodynamic limit). To this end, a qualitative difference between the one-third- and the one-sixth-filled cases becomes clear. In the one-sixth-filled case ($n = 1/3$), the effective Hamiltonian $\mathcal{H}_{\rm ring}$ connects all

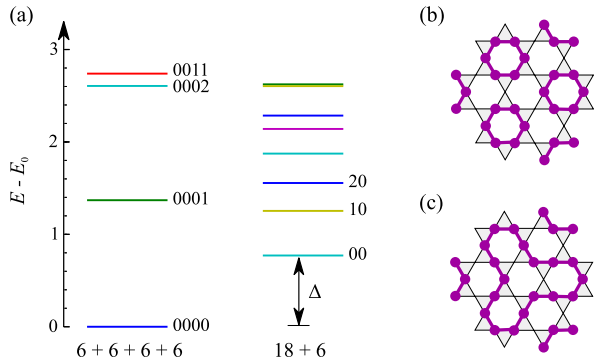


FIG. 5. (Color online) (a) Excitation energies of the spin Hamiltonian ($\mathcal{H}_{\rm spin}$) for two loop configurations of the 36-site cluster: one consisting of four short loops of length 6, and the other consisting of one 18-site loop and one 6-site loop. Numbers next to the levels indicate in which state each loop is; e.g., 0001 means that three loops are in the ground state and one is in the first excited spin state.

spin configurations within the zero winding sector yielding a ferromagnetic ground state [19].[1]

This is no longer the case for the one-third-filled case: the ground state is degenerate, and the ferromagnetic state and the singlet state are among the ground states. However, the dynamic subsystems $A$ and $B$ are still ferromagnetic: our system can be thought of as putting together two one-sixth-filled systems, each of them living on the $A$ and the $B$ dynamic sublattices of the ground-state manifold.

### B. Short loop phase ($\alpha = 0$)

At $\alpha = 0$, the effective Hamiltonian is reduced solely to $\mathcal{H}_{\rm spin}$. Since the fluctuations in electron occupation vanish, the ground state is the one which minimizes the spin exchange interactions along the closed electron loops. This is achieved with short hexagonal loops, giving rise to a 'short-loop phase," shown in Fig. 8 (left). The finite-size correction for the ground-state energy per site of a periodic antiferromagnetic Heisenberg chain of length $L$ is [27]

$$e_L - e_\infty = -\frac{\pi^2}{12L^2} \tag{10}$$

in the leading order in $1/L$, where $e_\infty = 1/4 - \ln 2 \approx -0.4431$ stands for the energy density in the thermodynamic limit. Thus, the shorter the loop is, the lower the energy density becomes. The shortest loop on the kagome lattice is of length $L = 6$ with energy $e_6 \sim -0.4343$, and these loops are arranged in a regular pattern, as shown in Fig. 5(b), with a hexagonal unit cell consisting of nine sites. This ground state is threefold degenerate and breaks the translational symmetry. The lowest energy excitation of this charge-ordered phase is realized by the formation of an $L = 18$ loop out of three adjacent hexagonal loops [Fig. 5(c)], with the energy gap $\Delta = E_{18} - 3E_6 = 0.771$. In Fig. 5(a) the energies of different charge (or loop) configurations in a 36-site cluster are shown.

## IV. NUMERICAL RESULTS

We have already found that the two extreme cases $\alpha = 0$ and $\alpha = 1$ show different orderings. The transition between the two phases can be understood by using the analogy to the quantum-dimer model on a honeycomb lattice.[2] As discussed in detail in Ref. [25], the two different orderings have centers of rotation symmetry that lie in distinct places when forming domains of one phase with the other (in fact, the precise nature of the phase transition might be either a first-order one or two phase transitions with coexisting order parameters, as suggested in Ref. [28] for the quantum-dimer model on a square lattice). Thus we expect a phase transition between them when tuning the parameter $\alpha$ from 0 to 1.

In order to pin down the transition and to verify the above-mentioned two characteristic phases, we employ numerical exact diagonalization of the effective Hamiltonian $H_{\rm eff}$ on finite clusters of $N = 27$ and 36 sites. We simulate $H_{\rm eff}$ within the Hilbert space spanned by the allowed configurations. Furthermore, we reduce the Hilbert-space size by making use of the spatial symmetries given in Appendix B. The results are summarized in Fig. 8, which shows the phase diagram we obtain from our numerical analysis: We observe a first-order phase transition from a short-loop to a plaquette-ordered phase at $\alpha \approx 0.6$. Both phases have a charge gap but only the former one has a spin gap. The details of the numerical simulations are described below.

However, before presenting our numerical findings, we mention that the strong-coupling limit of the Hubbard model (more precisely, the $tJ$ model) at the same filling as ours, but without the nearest-neighbor $V$ term, has been discussed in Ref. [18]. It has been found that the ground state is formed by a resonance of two electrons in the singlet state on disjunct triangles, making a crystal. The ground state is twofold degenerate, depending whether the resonances are taking place on the up- or down-pointing triangles. The crucial difference with respect to our model is that the number of electrons in the triangles can deviate from two in their model (there are two electron only in average). In fact, the electron number strongly fluctuates in the triangles connecting the resonating pairs, which costs energy due to the $V$ term and leads to destabilization of the state. The Hubbard model for the one-third-filling case has been studied in Ref. [17] using a Hartree-Fock mean-field theory which provided a rich phase diagram: Our short-loop phase can be recognized as the CDWIII phase in their work, while our plaquette phase is missing, as the quantum fluctuations stabilizing the resonance of charges are beyond the reach of the Hartree-Fock approach.

[1]This can be traced back to the number of fermions taking place in the effective ring exchange: For an odd number of fermions high spin is favored, while for an even number of electrons a low-spin state (singlet) is lower in energy, as, e.g., in Ref. [15] for a quarter-filled checkerboard lattice.

[2]Even though the effective Hamiltonian, (2), is more complex than the quantum-dimer model, they both have the same symmetry properties with respect to the charge degrees of freedom. The short-loop phase can be mapped to the columnar phase and the plaquette phases can be identified in both models.

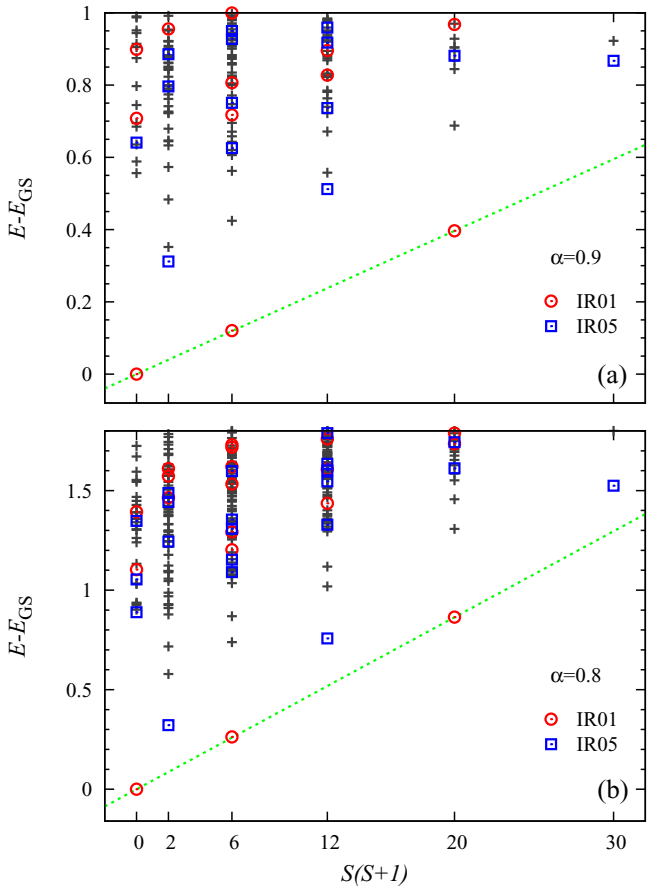


FIG. 6. (Color online) Anderson tower for the $N = 36$ cluster for (a) $\alpha = 0.9$ and (b) $\alpha = 0.8$. The energies of the two low-lying two series of states belonging to different irreducible representations, IR01 and IR05 (see Appendix B), which are even and odd with respect to $P_{AB}$, behave proportionally to $S(S+1)$. As $\alpha$ increases and/or the system size increases, their gradient decreases toward 0, at which all these points fall onto the same horizontal line (become degenerate). Such behavior is a strong indication of antiferromagnetic ordering.

### A. Anderson tower

As for the case $\alpha = 1$, we have seen that the conservation of the spin on the $A$ and $B$ dynamic sublattices leads to a degenerate ground state. The spins on the two dynamic sublattices take the maximal value $S_A = S_B = N/6$, and as they do not interact, the states spanned by the two "giant" spins constitute the ground-state manifold (Fig. 4 reveals that states with lower sublattice spins $S_A$ and $S_B$ are higher in energy). Once the $\mathcal{H}_{\rm spin}$ is turned on, the hidden conservation law no longer holds, and the spins on the $A$ and $B$ sublattices start to interact with each other:

$$\mathcal{H}_{\rm LM} \propto \frac{J}{N}\,\mathbf{S}_{\rm A}\cdot\mathbf{S}_{\rm B}, \tag{11}$$

similarly to a Lieb-Mattis model, as the kinetic term $g \gg J$ decouples the wave function and each spin on the $A$ sublattice interacts with each spin on the $B$ sublattice with an effective coupling $\propto J/N$. Denoting by $S_{\rm tot}$ the total spin of the system, the energy of this Hamiltonian is simply described as

$$\mathcal{E}_{\rm LM} \propto \frac{J}{N}[S_{\rm tot}(S_{\rm tot}+1) - S_A(S_A+1) - S_B(S_B+1)]. \tag{12}$$

Indeed, the degeneracies at $\alpha = 1$ are quickly removed with decreasing $\alpha$ (see Fig. 7). When plotted against $S_{\rm tot}(S_{\rm tot}+1)$, the spectrum shows low-energy states whose energy is $\propto J/N\,S_{\rm tot}(S_{\rm tot}+1)$, as shown in Fig. 6. These states form the Anderson tower, which is the clear signature of an antiferromagnetic ordering [29]. In this case, the texture of the antiferromagnetic order is quite peculiar, as schematically shown in Fig. 8 (right): a large effective spin-3/2 of resonating charges on a hexagon is surrounded by "localized" spin-1/2 electrons. The resonating plaquette can occupy either of the three inequivalent hexagon sublattices, thus the state is threefold degenerate regarding the space-group symmetries. This is reflected in the irreducible content of the states in the Anderson tower in Fig. 6; IR1 and IR5 for the 36-site cluster (see Appendix B for the whole chart of the irreducible representation). With increasing system size, the slope of the lowest energy levels approaches 0 as $1/N$ and becomes degenerate in the thermodynamic limit. The finite-size gap of the states above the Anderson tower also goes to 0; in the case of antiferromagnetic ordering we expect that the scaling follows $1/\sqrt{N}$, which, however, could not be checked in our problem due to the rapidly growing dimension of the Hilbert space. The spin excitation spectrum becomes gapless, in contrast to the short-loop phase when $\alpha \approx 0$.

### B. Energy spectrum

We now consider the ground state and lowest excited states over the full range $\alpha \in [0,1]$. Figure 7 shows the energy spectra as a function of $\alpha$ for the clusters with $N = 27$ and 36 sites. At $\alpha = 0$, the excitation gap above the threefold degenerate ground state corresponds exactly to the value of $\Delta$ obtained by diagonalizing the Heisenberg chains in Sec III. Due to finite-size effects, the threefold degeneracy of the ground state is lifted immediately for any $\alpha > 0$. A level crossing in the lowest excitations is prominent near $\alpha = 0.6$ for both clusters, indicating that the system undergoes a first-order quantum phase transititon [30–32].

Combining the findings in the previous sections and the exact diagonalization data in Fig. 7, we reach the phase diagram shown in Fig. 8. Two phases are separated by a first-order phase transition; for $\alpha \lesssim 0.6$ we find the short-loop phase, representing a charge-ordered phase that has both a charge and a spin gap.

### C. Correlation functions and structure factors

We calculate several different kinds of correlation functions for the $N = 36$ cluster which serve as characteristic fingerprints of the phases. We begin by studying the charge-charge correlation functions,

$$C^c(\mathbf{r}_0,\mathbf{r}_j) = \langle n(\mathbf{r}_0)n(\mathbf{r}_j)\rangle - \langle n(\mathbf{r}_0)\rangle\langle n(\mathbf{r}_j)\rangle, \tag{13}$$

where $\mathbf{r}_0$ and $\mathbf{r}_j$ are the positions of charges on the kagome lattice and the expectation values are taken with respect to

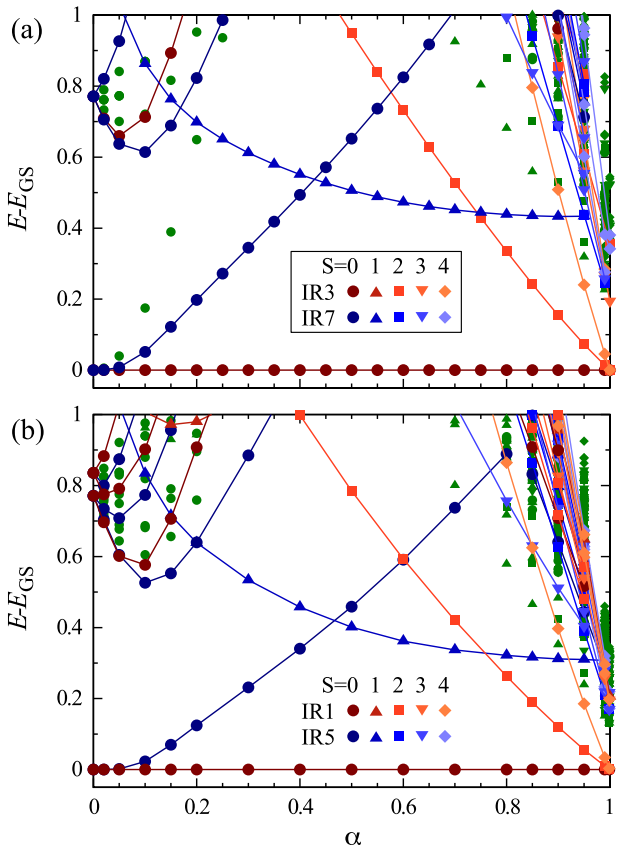


FIG. 7. (Color online) Energy spectra for two clusters, $N = 27$ in (a) and $N = 36$ in (b). The level crossing occurs at $\alpha_c \approx 0.6$ between the energy levels of the same quantum number for both clusters, which indicates a possible quantum phase transition. All energies are measured from the lowest energy singlet state.

the ground state. $n(\mathbf{r}_j)$ is the occupation number operator, which measures whether the charge is present at $\mathbf{r}_j$ regardless of its spin orientation. Figure 9(a) shows the density plot of $C^c(\mathbf{r}_0,\mathbf{r}_j)$ at $\alpha = 0$, which describes the charge order of the short-loop phase. The charges on the hexagons, which form short loops, are perfectly correlated. With increasing $\alpha$, this order gradually melts toward $\alpha = 1$, at which only the short-range correlations remain as shown in Fig. 9(b). The

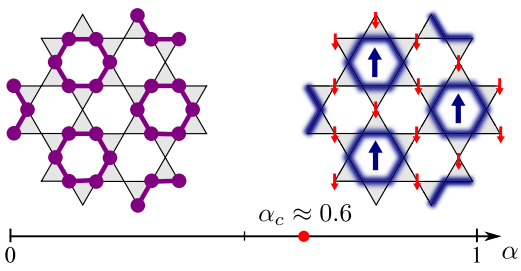


FIG. 8. (Color online) Ground-state phase diagram of Eq. (2). With increasing $\alpha$, the short-loop phase undergoes a first-order quantum phase transition into the plaquette phase at around $\alpha \sim 0.6$. The purple hexagons in the left panel denote the short loops formed by neighboring electrons, and blurred blue hexagons in the right panel indicate the presence of resonating plaquettes.

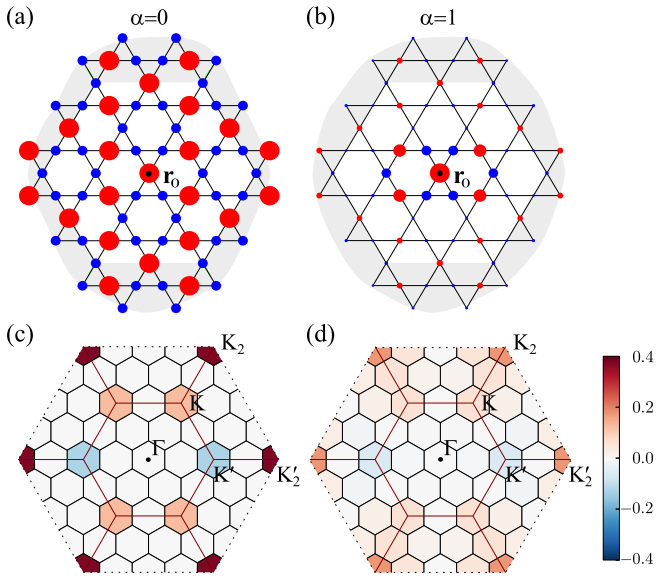


FIG. 9. (Color online) (a), (b) Charge-charge correlation function in real space for $\alpha = 0$ and 1, respectively. Correlations are calculated with respect to the marked site $\mathbf{r_0}$ at the center. The radius of the dots is proportional to the absolute value of the correlation, while the color encodes the sign (red corresponds to a positive value; blue, to a negative value). (c), (d) The same data in momentum space in the extended Brillouin zone. The maximum in (c) is found at $\mathbf{Q} = (8\pi/3,0)$ and symmetry-related points (high-symmetry points denoted $K_2$ and $K_2'$).

corresponding structure factor,

$$S^c(\mathbf{q}) = \frac{1}{N}\sum_j e^{-i\mathbf{q}\cdot(\mathbf{r}_j-\mathbf{r}_0)}\, C^c(\mathbf{r}_0,\mathbf{r}_j), \tag{14}$$

is calculated in the extended Brillouin zone as shown in Fig. 9. Note that we do not average the structure factor over the entire unit cell but instead calculate it for a specific center. Thus we have both positive and negative contributions. In experiments, one would observe the averaged structure factor. The ordering wave vectors $\mathbf{Q}$ of the short-loop phase lie at the corners ($K_2$ and $K_2'$) of the extended Brillouin zone, where the sharp peaks are observed.

Next we consider the plaquette-plaquette correlation function

$$C^h(\mathbf{R}_0,\mathbf{R}_j) = \langle h_{\hexagon}(\mathbf{R}_0) h_{\hexagon}(\mathbf{R}_j)\rangle - \langle h_{\hexagon}(\mathbf{R}_0)\rangle\langle h_{\hexagon}(\mathbf{R}_j)\rangle, \tag{15}$$

where the operators $h_{\hexagon}(\mathbf{R}_0)$ and $h_{\hexagon}(\mathbf{R}_j)$ are those representing the resonance, as defined in Eq. (4), on hexagons centered at positions $\mathbf{R}_0$ and $\mathbf{R}_j$, respectively. The centers of these hexagons form a triangular lattice. At $\alpha = 0$, $C^h(\mathbf{R}_0,\mathbf{R}_j)$ vanishes except for $\mathbf{R}_0 = \mathbf{R}_j$, as shown in Fig. 10(a). This is because the charges are perfectly localized on short loops and, thus, cannot resonate. By contrast, we find a clear sign of the plaquette ordering at $\alpha = 1$ in Fig. 10(b), whose spacial pattern is exactly the one expected in Fig. 8. The structure factor $S^h(\mathbf{Q})$ for both cases is calculated analogously to Eq. (14) and is

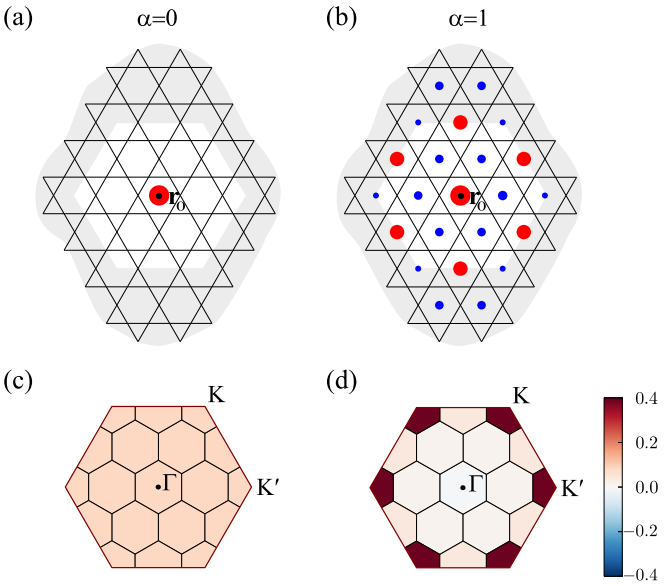


FIG. 10. (Color online) (a), (b) Plaquette-plaquette correlation function in real space for $\alpha = 0$ and 1, respectively. Correlations are calculated with respect to the marked site $\mathbf{r_0}$ at the center. The radius of the dots is proportional to the absolute value of the correlation, while the color encodes the sign (red corresponds to a positive value; blue, to a negative value). (c), (d) The same data in momentum space in the first Brillouin zone. The peaks in (d) are found at the $K$ and $K'$ points, with $\mathbf{Q} = (2\pi/3, 2\pi/\sqrt{3})$ and $\mathbf{Q} = (4\pi/3, 0)$, respectively.

displayed over the first Brillouin zone in Figs. 10(c) and 10(d). The one at $\alpha = 0$ is structureless, whereas at $\alpha = 1$ we observe sharp peaks at the corners of the first Brillouin zone.

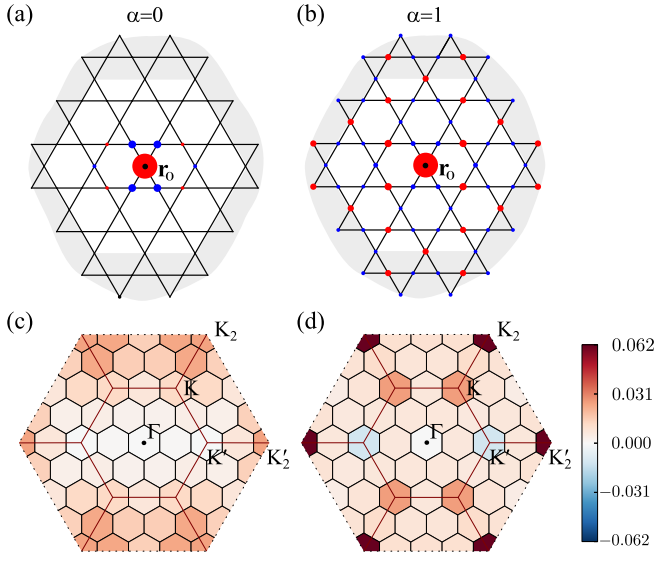


FIG. 11. (Color online) (a), (b) Spin-spin correlation function in real space for $\alpha = 0$ and 1, respectively. Correlations are calculated with respect to the marked site $\mathbf{r_0}$ at the center. The radius of the dots is proportional to the absolute value of the correlation, while the color encodes the sign (red corresponds to a positive value; blue, to a negative value). (c), (d) The same data in momentum space in the extended Brillouin zone.

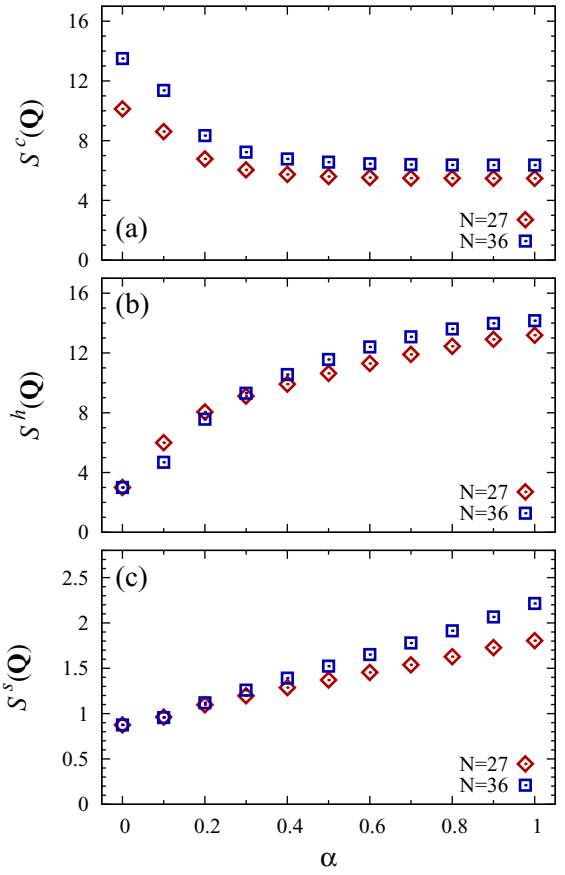


FIG. 12. (Color online) Amplitudes of the (a) charge, (b) plaquette, (c) and spin structure factors, shown in Figs. 9–11, at the corresponding ordering wave vectors $\mathbf{Q}$. The gradual changes in all panels indicate the melting of different kinds of ordering as the parameter $\alpha$ is varied.

Finally, we consider the spin-spin correlation function,

$$C^s(\mathbf{r}_0, \mathbf{r}_j) = \langle \mathbf{S}(\mathbf{r}_0)\mathbf{S}(\mathbf{r}_j)\rangle - \langle \mathbf{S}(\mathbf{r}_0)\rangle\langle \mathbf{S}(\mathbf{r}_j)\rangle, \qquad (16)$$

where the operator $\mathbf{S}_{\mathbf{r}_j}$ is the spin-1/2 spin operator at site $\mathbf{r}_j$. For $\alpha = 0$ the spins living on different short loops are uncorrelated, and this is clearly seen in $C^s(\mathbf{r}_0, \mathbf{r}_j)$, which vanishes once the distance is $|\mathbf{r}_0 - \mathbf{r}_j| > 2$ [Fig. 11(a) and its corresponding structure factor in Fig. 11(c)]. The spin structure becomes more distinct as $\alpha$ goes to 1 [see Figs. 11(b) and 11(d)], and its textures in real and reciprocal spaces follow those of the charge in Figs. 9(b) and 9(d). As discussed earlier, the spins living on two dynamic sublattices form large ferromagnetic spins, $S_A$ and $S_B$, and one would find large correlations between the spins belonging to the same sublattice, if the dynamic sublattice could be extracted. However, in real space, the strong change fluctuations will cause the mixing of the two dynamic sublattices, and quite a large portion of the real-space correlations is canceled out.

In Fig. 12 we show how the amplitudes of different structure factors at the respective ordering wave vectors (the $\mathbf{Q}$ point, which has the highest amplitude of the structural factors) evolve. Here we multiply the amplitudes by the system size $N$,

in order to compare the results of different sizes on the same ground, assuming that the sum rules are fulfilled. While the general tendency is clear, it is difficult to identify the phase transition point between the two phases in the correlation functions, presumably due to the finite-size effect.

## V. SUMMARY AND OUTLOOK

We have considered a system of strongly correlated electrons on a kagome lattice at one-third filling and focused on the interplay of charge and spin fluctuations. A surprising aspect of our findings is that the originally complicated correlation and dynamics of the charge and spin degrees of freedom could be well separated within our approach in the strong-coupling limit. We have derived an effective Hamiltonian which acts on a low-energy manifold consisting of configurations with exactly two electrons per each triangle of the kagome lattice with no double-occupancy.

We have discussed in detail two limiting cases: (i) In the limit where charge fluctuations dominate, a robust resonating "plaquette ordered" phase is found. The charge fluctuations conserve the magnetization on two dynamical sublattices and maximize the total spin in each sector [19], yielding a huge degeneracy. Small spin fluctuations then couple two giant spins weakly, leading to gapless spin excitations. (ii) In the limit where spin fluctuations dominate, the electrons are confined to short loops around the hexagons to maximize the energy gain due to spin fluctuations.

Using large-scale exact diagonalization, we have evaluated the phase diagram and found a first-order transition separating the "plaquette-ordered" and the "short-loop" phase. For both phases we obtained the fingerprints in the form of experimentally accessible signatures like spin and charge structure factors.

To find the physics we discuss in this paper, we need to search for strongly correlated materials with a kagome lattice structure in the mixed-valence regime. This might possibly be achieved by heavy doping of current kagome spin-liquid candidates like $ZnCu_3(OH)_6Cl_2$ [33,34] and $Rb_2Cu_3SnF_{12}$ [35] to get the desired filling factors.

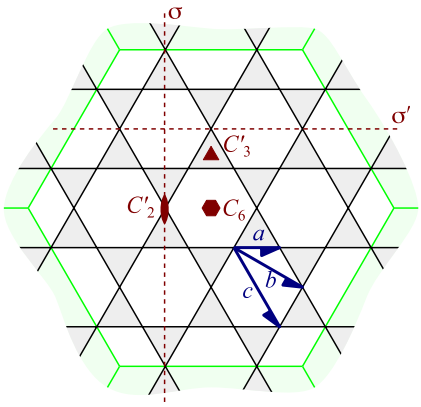


FIG. 13. (Color online) Description of a cluster with $N = 36$ sites and periodic boundary conditions. The symmetries of the point group are shown in dark red: the hexagon denotes the rotation center of order 6 ($C_6$); the triangle, the rotation center of order 3 ($C'_3$); and the oval, the rotation center of order 2 ($C'_2$). Dashed lines are the reflections $\sigma$ and $\sigma'$. Dark-blue lines with half-arrows denote glide reflections.

*Note added in proof.* Recently we learned about a similar work by K. Ferhat and A. Ralko [36]: they considered the Hubbard model, Eq. (1), without mapping to an effective model and reached conclusions similar to ours for the considered limit.

## ACKNOWLEDGMENTS

K.P. and C. H. gratefully acknowledge the hospitality of the guest program of MPI-PKS Dresden, where much of this work was carried out. The authors thank Peter Fulde and Andreas Läuchli for stimulating discussions. This work was supported by Grant-in-Aid for Scientific Research No. 25800204 from the Ministry of Education, Science, Sports and Culture of Japan and by Hungarian OTKA Grant No. 106047.

TABLE I. Character table for the 36-site cluster.

| IR | I | $6\sigma$ | $18\sigma'$ | $9C'_2$ | $3C_6^3$ | $6T_1$ | $12c$ | $12a$ | $18b$ | $6a^3$ | $3T_1T_2$ | $2T_1^2$ | $24C_6$ | $16C'_3$ | $8C_6^2$ | BZ |
|---|---|---|---|---|---|---|---|---|---|---|---|---|---|---|---|---|
| 1 | 1 | 1 | 1 | 1 | 1 | 1 | 1 | 1 | 1 | 1 | 1 | 1 | 1 | 1 | 1 | Γ |
| 2 | 1 | 1 | −1 | −1 | −1 | 1 | 1 | 1 | −1 | 1 | 1 | 1 | −1 | 1 | 1 | Γ |
| 3 | 1 | −1 | 1 | −1 | −1 | 1 | −1 | −1 | 1 | −1 | 1 | 1 | −1 | 1 | 1 | Γ |
| 4 | 1 | −1 | −1 | 1 | 1 | 1 | −1 | −1 | −1 | −1 | 1 | 1 | 1 | 1 | 1 | Γ |
| 5 | 2 | 2 | 0 | 0 | 0 | −1 | −1 | −1 | 0 | 2 | 2 | −1 | 0 | −1 | 2 | *K* |
| 6 | 2 | −2 | 0 | 0 | 0 | −1 | 1 | 1 | 0 | −2 | 2 | −1 | 0 | −1 | 2 | *K* |
| 7 | 2 | 0 | 0 | 2 | 2 | 2 | 0 | 0 | 0 | 0 | 2 | 2 | −1 | −1 | −1 | Γ |
| 8 | 2 | 0 | 0 | −2 | −2 | 2 | 0 | 0 | 0 | 0 | 2 | 2 | 1 | −1 | −1 | Γ |
| 9 | 4 | 0 | 0 | 0 | 0 | −2 | 0 | 0 | 0 | 0 | 4 | −2 | 0 | 1 | −2 | *K* |
| 10 | 3 | 1 | 1 | −1 | 3 | −1 | 1 | −1 | −1 | −1 | −1 | 3 | 0 | 0 | 0 | *M* |
| 11 | 3 | 1 | −1 | 1 | −3 | −1 | 1 | −1 | 1 | −1 | −1 | 3 | 0 | 0 | 0 | *M* |
| 12 | 3 | −1 | 1 | 1 | −3 | −1 | −1 | 1 | −1 | 1 | −1 | 3 | 0 | 0 | 0 | *M* |
| 13 | 3 | −1 | −1 | −1 | 3 | −1 | −1 | 1 | 1 | 1 | −1 | 3 | 0 | 0 | 0 | *M* |
| 14 | 6 | 2 | 0 | 0 | 0 | 1 | −1 | 1 | 0 | −2 | −2 | −3 | 0 | 0 | 0 | |
| 15 | 6 | −2 | 0 | 0 | 0 | 1 | 1 | −1 | 0 | 2 | −2 | −3 | 0 | 0 | 0 | |

## APPENDIX A: PROOF FOR THE DYNAMIC SUBLATTICE RULE

In this Appendix we prove that the effective ring-exchange Hamiltonian ($\alpha = 1$) conserves the magnetization on dynamic sublattices. The rules for the "dynamic sublattice" are simple: (i) neighboring electrons have different sublattice labels and (ii) next-nearest-neighbor electrons have the same sublattice label on each hexagon of the kagome lattice. Once we have the configuration which fulfills (i) and (ii), the effective Hamiltonian $\mathcal{H}_{\text{ring}}$ preserves this rule. A flippable hexagon involves necessarily only loop segments of the same kind demanded by (ii). Also, the protruding bonds coming out of a flippable hexagon are always exactly of the opposite kind to that which the hexagon is made of. Let us assume without loss of generality an $A$-$A$-$A$ configuration on the flipped hexagon. Then the six protruding bonds will essentially be labeled $B$. Flipping the loop segments around a hexagon does not change the positions relative to each other and thus (i) and (ii) are fulfilled in the resulting hexagon configuration. Next we have to check the six neighboring hexagons. The three hexagons which lose a loop segment trivially fulfill the conditions. For hexagons which gain a loop segment, we need to argue a little more. The neighboring links of the added segment are necessarily occupied by a $B$ segment since the initial configuration was a valid closely packed loop configuration and it fulfilled (i). Since the neighboring segments are of the $B$ type, we know that the next-nearest-neighbor segments are of the $A$ type or empty. Thus the resulting configuration fulfills (i) and (ii).

## APPENDIX B: IRREDUCIBLE REPRESENTATION OF THE 36-SITE CLUSTER

The symmetry-group elements of the 36-site cluster with periodic boundary conditions are shown in Fig. 13. The symmetry group of the kagome lattice is the wallpaper group **p6m**, with the point group $\mathcal{D}_6$. The 36-site cluster consists of 12 unit cells, and since the order of the $\mathcal{D}_6$ is 12, the total number of the symmetry group elements is $12 \times 12 = 144$. Table I is the character table for the 36-site cluster, where we also specify the point(s) in the Brillouin zone to which it belongs (Table I).


[1] C. Castelnovo, R. Moessner, and S. L. Sondhi, Nature **451**, 42 (2008).
[2] R. Moessner and S. L. Sondhi, Phys. Rev. B **68**, 184512 (2003).
[3] M. Hermele, M. P. A. Fisher, and L. Balents, Phys. Rev. B **69**, 064404 (2004).
[4] N. Shannon, O. Sikora, F. Pollmann, K. Penc, and P. Fulde, Phys. Rev. Lett. **108**, 067204 (2012).
[5] O. Benton, O. Sikora, and N. Shannon, Phys. Rev. B **86**, 075154 (2012).
[6] P. Mendels and A. S. Wills, in *Introduction to Frustrated Magnetism*, *Springer Series in Solid-State Sciences,* Vol. 164, edited by C. Lacroix, P. Mendels, and F. Mila (Springer, Berlin, 2011), pp. 207–238.
[7] S. Yan, D. A. Huse, and S. R. White, Science **332**, 1173 (2011).
[8] S. Depenbrock, I. P. McCulloch, and U. Schollwöck, Phys. Rev. Lett. **109**, 067201 (2012).
[9] H.-C. Jiang, Z. Wang, and L. Balents, Nature Phys. **8**, 902 (2012).
[10] S. Nishimoto, N. Shibata, and C. Hotta, Nat. Commun. **4**, 2287 (2013).
[11] P. Fulde, K. Penc, and N. Shannon, Ann. Physik **11**, 892 (2002).
[12] E. Runge and P. Fulde, Phys. Rev. B **70**, 245113 (2004).
[13] F. Pollmann and P. Fulde, EPL (Europhys. Lett.) **75**, 133 (2006).
[14] A. O'Brien, F. Pollmann, and P. Fulde, Phys. Rev. B **81**, 235115 (2010).
[15] D. Poilblanc, K. Penc, and N. Shannon, Phys. Rev. B **75**, 220503 (2007).
[16] F. Trousselet, D. Poilblanc, and R. Moessner, Phys. Rev. B **78**, 195101 (2008).
[17] J. Wen, A. Rüegg, C.-C. J. Wang, and G. A. Fiete, Phys. Rev. B **82**, 075125 (2010).
[18] M. Indergand, A. Läuchli, S. Capponi, and M. Sigrist, Phys. Rev. B **74**, 064429 (2006).
[19] F. Pollmann, P. Fulde, and K. Shtengel, Phys. Rev. Lett. **100**, 136404 (2008).
[20] P. W. Anderson, Phys. Rev. **102**, 1008 (1956).
[21] M. E. Fisher and J. Stephenson, Phys. Rev. **132**, 1411 (1963).
[22] K. Penc, H. Shiba, F. Mila, and T. Tsukagoshi, Phys. Rev. B **54**, 4056 (1996).
[23] A. Mielke, J. Phys. A: Math. Gen. **25**, 4335 (1992).
[24] A. Mielke and H. Tasaki, Commun. Math. Phys. **158**, 341 (1993).
[25] R. Moessner, S. L. Sondhi, and P. Chandra, Phys. Rev. B **64**, 144416 (2001).
[26] D. S. Rokhsar and S. A. Kivelson, Phys. Rev. Lett. **61**, 2376 (1988).
[27] F. Woynarovich and H.-P. Eckle, J. Phys. A: Math. Gen. **20**, L97 (1987).
[28] A. Ralko, D. Poilblanc, and R. Moessner, Phys. Rev. Lett. **100**, 037201 (2008).
[29] B. Bernu, C. Lhuillier, and L. Pierre, Phys. Rev. Lett. **69**, 2590 (1992).
[30] S. Sachdev, *Quantum Phase Transitions* (Wiley Online Library, 2007).
[31] N. V. Zamfir, P. von Brentano, R. F. Casten, and J. Jolie, Phys. Rev. C **66**, 021304 (2002).
[32] J. M. Arias, J. Dukelsky, and J. E. Garcia-Ramos, Phys. Rev. Lett. **91**, 162502 (2003).
[33] P. Mendels and F. Bert, J. Phys. Soc. Jpn. **79**, 011001 (2010).
[34] T.-H. Han, J. S. Helton, S. Chu, D. G. Nocera, J. A. Rodriguez-Rivera, C. Broholm, and Y. S. Lee, Nature **492**, 406 (2012).
[35] K. Morita, M. Yano, T. Ono, H. Tanaka, K. Fujii, H. Uekusa, Y. Narumi, and K. Kindo, J. Phys. Soc. Jpn. **77**, 043707 (2008).
[36] K. Ferhat and A. Ralko, Phys. Rev. B **89**, 155141 (2014).